Electron scattering at Ru-TiN-Ru interface stacks, Poyen Shen and Daniel Gall, IEEE Trans. Electron Devices ***71****, 6970 (2024)*.https://dx.doi.org/10.1109/TED.2024.3453223

Electron scattering at Ru-TiN-Ru interface stacks

Poyen Shen and Daniel Gall

***Abstract*—Electron transport across Ru-TiN-Ru interfaces is quantified using multilayers containing five 10-nm-thick Ru(0001) layers separated by TiN interlayers with nominal thicknesses d_{TiN} ranging from 0.01-1.6 nm. The multilayers are deposited by sputtering on Al_2O_3(0001) substrates at 700 °C. Their resistivity parallel to the interfaces increases linearly from ρ = 7.8 to 11.2 μΩ-cm with increasing d_{TiN} = 0 - 0.2 nm and saturates at a constant ρ = 13.3 ± 2.5 μΩ-cm for $d_{TiN} \geq$ 0.4 nm. The linear increase is attributed to electron impurity scattering at a discontinuous TiN layer while resistivity saturation is associated with parallel conduction in individual Ru layers without coherent transport between Ru layers. The data indicate a critical d_{TiN} = 0.4-0.6 nm above which electron transport across Ru-TiN-Ru is completely diffuse, leading to a Ru-TiN-Ru contact resistance that is proportional to the TiN layer thickness. This critical thickness is in good agreement with the onset d_{TiN} = 0.4-0.6 nm of a decrease in the out-of-plane x-ray coherence length, the onset at d_{TiN} = 0.4 nm of a detectable x-ray diffraction superlattice peak, and the development of x-ray reflectivity superlattice fringes for $d_{TiN} \geq$ 0.4 nm.**

***Index Terms*—Interconnects, Ru-TiN materials, electron transport**

I. Introduction

A major challenge for the continued downscaling of features in integrated circuits is the signal delay and power consumption caused by an increasing interconnect resistance with decreasing critical dimensions, caused by both a decreasing cross-sectional area [1], [2] and an increasing resistivity [3]–[6]. The resistivity increase is due to electron scattering at surfaces [7]–[12], interfaces [13]–[18], and grain boundaries [19]–[24], and motivates extensive ongoing research that quantifies the conductance of alternative materials solutions for the most scaled interconnects [25]–[29]. This includes the Ru/TiN conductor/liner system, where Ru is promising because of its low mean free path and high melting point (2250 °C), resulting in a low resistivity size effect [25], [29]–[31] and a high temperature and electromigration stability [10], [25], while TiN with its relatively low electrical resistivity and high chemical stability enhances Ru adhesion, reliability, processing and nucleation [13], [14], [32]–[34]. The resistance of an interconnect stack includes the contact resistance between horizontal line and vertical via wires. This contact represents a potential resistance bottleneck, as the current needs to travel across the liner which typically has a much larger resistivity than the metal. Thus, the resistance of the metal-liner-metal interface becomes an important quantity to be considered during back-end-of-line materials selection decisions, which motivates the present study on the Ru-TiN-Ru contact resistance.

In this paper, we study electron scattering at Ru-TiN-Ru interfaces using transport measurements parallel to the interfaces of Ru-TiN multilayer stacks. Transport measurements parallel to the interfaces are an effective approach to quantify metal-metal interface transport because they do not require contacting at nm-dimensions as would be required for direct current measurements across the interfaces. We have recently demonstrated this approach to determine the contact resistance of epitaxial W(001)/Mo(001) [35] interfaces. Here we measure the resistivity of approximately 50-nm-thick Ru-TiN multilayer films as a function of the thickness d_{TiN} = 0-1.6 nm of four TiN interlayers that separate five 10-nm thick Ru metal films. The multilayers are grown on c-plane sapphire substrates and encapsulated at the bottom and top by 2-nm-thick TiN layers, that is, a 2-nm-thick TiN layer separates bottom Ru layer from the substrate and the while another TiN layer protects the top Ru layer from air exposure. The multilayer resistivity increases with d_{TiN} up to a critical thickness of 0.4-0.6 nm which represents the maximum effective TiN thickness for partially coherent electron transport across the Ru-TiN-Ru interface. This critical thickness matches the measured onset d_{TiN} = 0.4-0.6 nm of a decrease in the out-of-plane x-ray coherence length, detectable x-ray diffraction superlattice peaks at d_{TiN} = 0.4 and 0.6 nm, and the onset for x-ray reflectivity superlattice fringes at d_{TiN} = 0.4 nm. These results show that the Ru-TiN-Ru contact resistance is dominated by the TiN resistivity and

The authors acknowledge funding from the Semiconductor Research Corporation (SRC) under task 3085.001, SRC/DARPA under JUMP 2.0 center tasks 3137.019 and 3137.021, the National Science Foundation (NSF) under grant No. 2328906 through the Future of Semiconductors program supported by NSF and industry partners, and from the NY State Empire State Development's Division of Science, Technology and Innovation (NYSTAR) through Focus Center-NY–RPI Contract C180117.. The authors are with the Department of Materials Science and Engineering, Rensselaer Polytechnic Institute, 110 8th St, Troy, NY 12180, USA. Corresponding author: Daniel Gall; email: galld@rpi.edu

is proportional to d_{TiN} if d_{TiN} is larger than the critical thickness.

II. Experimental procedure

Ru-TiN multilayers stacks were deposited on Al_2O_3(0001) substrates in an ultra-high vacuum DC magnetron sputter deposition system with a base pressure of 10^{-9} Torr [36]. One-side polished 10×10×0.5 mm^3 Al_2O_3(0001) wafers were cleaned in subsequent ultrasonic baths of Hellmanex solution, acetone, isopropyl alcohol, and de-ionized water for 15 mins each, attached to a molybdenum block with colloidal silver paint, inserted into the deposition system through a load lock, and degassed in vacuum at 800 °C for one hour, using a radiative pyrolytic graphite heater. Ru metal depositions were done in 10 mTorr 99.999% pure Ar while TiN depositions were done by reactive sputtering in a 7.5 mTorr 99.999% pure N_2 working gas. All depositions were done at a constant temperature T_s = 700 °C. This temperature was chosen to simultaneously maximize crystalline quality of both Ru and TiN, as determined by x-ray diffraction on individual Ru and TiN films, which are epitaxial hcp Ru(0001) and approximately stoichiometric rock-salt structure TiN(111), respectively. 5-cm-diameter 99.95% pure ruthenium and 99.995% pure titanium targets were facing a continuously rotating substrate at a 12 cm distance and at -45° and 45° tilts. They were sputter cleaned prior to deposition for 10 min with closed shutters. Subsequently, the shutters in front of the Ru and Ti targets were alternately opened and closed, and the working gas was switched, to obtain alternate deposition of Ru and TiN layers, resulting in the desired multilayers. The time for adjusting the shutters and switching the gas was limited to < 30 sec to minimize possible contamination at the Ru-TiN interfaces from residual H_2O vapor. Constant dc powers of 38 and 20 W to the Ru and Ti targets, respectively, resulted in deposition rates of 0.14 nm/s Ru and 0.0015 nm/s TiN. The low TiN deposition rate was chosen to control ultra-thin (sub-monolayer) TiN deposition. The top and bottom of each multilayer stack are TiN layers with a fixed 2 nm thickness. This capping of the Ru layers removes possible confounding effects from electron scattering at Ru/substrate and/or Ru/air interfaces on electron transport. Each Ru interlayer was deposited for a total time of 144 s, yielding the same 10 nm nominal Ru film thickness, and a total thickness of five Ruthenium interlayers of 50 nm. The deposition time of the four TiN interlayers was varied from 7 to 1063 s, resulting in nominal TiN thicknesses d_{TiN} = 0.01–1.6 nm.

X-ray diffraction (XRD) analyses were performed using a PANalytical X'pert PRO MPD system with a $\lambda_{K\alpha}$ = 1.5418 Å Cu source with a fixed 0.5° divergence slit and a PIXcel solid-state line detector operating in scanning mode with a 14 mm active length corresponding to 255 active channels. ω rocking curves of Ru 0002 reflections were obtained using a parabolic mirror yielding a parallel beam with a < 0.055° divergence and a PIXcel solid-state line detector operating in receiving mode with a 0.165 mm active length using a fixed 2θ = 42.20°. X-ray reflectivity (XRR) measurements were performed with the same parallel beam x-ray optics used for ω scans. The measured XRR data were analyzed using the PANalytical X'Pert Reflectivity software which employs the Parratt formalism. The model for data fitting included alternating Ru and TiN layers on Al_2O_3, with densities fixed to literature values of 12.2, 5.4, and 3.95 g/cm^3, respectively. The free fitting parameters were the thickness of each layer within the multilayer stack and the roughness of each interface and top surface. These parameters were limited to ± 10% of the expected thicknesses and to < 2.0 nm for the roughness of each interface.

Transport measurements were done in air at 293 K with a linear four-point-probe with spring loaded tips and a 1.0 mm inter-probe spacing. The multilayer sheet resistance was obtained by applying the appropriate geometric correction factor [37] and the resistivity was determined from the measured sheet resistance by multiplying with the total (50 nm) Ru thickness of the five 10-nm-thick Ru layers, neglecting both the TiN thickness and the current in the TiN.

III. Results and Discussion

Figure. 1 shows X-ray diffraction θ-2θ patterns from six Ru-TiN multilayer stacks. Each stack contains five 10-nm-thick Ru layers as illustrated in the schematic at the left top. The six patterns are from stacks with different TiN interlayer thicknesses d_{TiN} = 0 – 1.0 nm, as labeled. Their intensity is plotted in a logarithmic scale and the patterns are offset by factors of 10 for clarity purposes. The d_{TiN} = 0 nm sample is a film without TiN interlayer, consisting of a 50-nm-thick Ru layer between 2-nm-thick TiN layers at the bottom and top. Its pattern shows a double-peak feature at 2θ = 41.70° and 41.80° due to the Al_2O_3 0006 substrate reflections of the $CuK_{\alpha1}$ and $CuK_{\alpha2}$ lines. The peak at 2θ = 42.25° is attributed to Ru 0002 and corresponds to an out-of-plane lattice parameter of 0.4280 nm. This is 0.2% smaller than the reported 0.4287 nm for relaxed hcp Ru, indicating a slight out-of-plane compressive strain caused by an in-plane tensile stress. It is the only film peak detected over the entire measured 2θ = 10-80° range, indicating a Ru 0001 alignment along the growth direction. The shoulders at 2θ = 40-41° are an experimental artifact associated with electronic noise in the line detector within 1.5° 2θ of the strong substrate and layer reflections. The patterns from the d_{TiN} = 0.1 and 0.2 nm samples are both qualitatively and quantitatively similar to the d_{TiN} = 0.0 nm pattern, exhibiting Ru 0002 peaks at 2θ = 42.20° and 42.19°, which indicate 0.05%

and 0.03% out-of-plane compressive strains, respectively. In contrast, the d_{TiN} = 0.4 nm pattern shows a new feature at 2θ = 42.94°, labeled with a brown arrow in Fig. 1. It is a superlattice satellite peak which is $\Delta 2\theta$ = 0.79° to the right of the main Ru 0002 peak, indicating a coherent Ru thickness of 18.0 nm. This is close to the nominal 20.4 nm total thickness of two neighboring Ru layers, including the 0.4 nm TiN interlayer. Thus, the superlattice peak appearing for d_{TiN} = 0.4 nm suggests that the nominally 0.4-nm-thick TiN interlayers are sufficient to disturb the Ru lattice so that it appears no longer as a coherent 50-nm-thick crystal but as five distinct Ru layers and, more specifically, neighboring Ru layers may still form coherency leading to a coherent thickness of 18.0 nm. In addition, the Ru 0002 peak from this pattern is 2% wider than for $d_{TiN} \leq 0.2$ nm, indicating the onset of a decreasing coherence length as discussed below. This trend continues for the d_{TiN} = 0.6 nm pattern which exhibits a 13% wider Ru 0002 peak and a superlattice peak at 2θ = 42.84°, corresponding to a coherent Ru thickness of 20.6 nm, matching perfectly the nominal thickness of two neighboring Ru layers plus the 0.6 nm Ti interlayer. This is also confirmed by a weak 2nd-order superlattice oscillation at 2θ = 43.70° of the d_{TiN} = 0.6 nm pattern. The Ru 0002 reflection for both d_{TiN} = 0.4 and 0.6 nm is at 2θ = 42.15°, corresponding to an out-of-plane lattice parameter of 0.4290 nm and a slight 0.06% tensile strain. That is, increasing d_{TiN} leads to a sign-change in the strain, suggesting that the TiN interlayers may facilitate relaxation of the Ru lattice. The d_{TiN} = 1.0 nm pattern has a much broader Ru 0002 peak, indicating that the coherency between the five Ru layers is considerably perturbed. It is so wide that its tail makes the expected superlattice peak no longer distinguishable from the background.

The Ru 0002 peak width is quantitatively analyzed in the right inset of Fig. 1, which shows a plot of the x-ray coherence length ξ vs d_{TiN}. It is obtained from the full-width-at-half-maximum (FWHM) of the Ru 0002 peak using $\xi = \lambda/(\sigma \cos\theta)$, where λ is the x-ray wavelength, σ is the FWHM and 2θ is Bragg's angle for the Ru 0002 reflection. The data points are colored according to the patterns in the main plot of Fig. 1. Black data points are from additional samples for which the θ-2θ pattern is not shown. The six samples with $d_{TiN} \leq 0.2$ nm have nearly identical ξ values, ranging from 39.0-41.2 nm, with an average 40.3 nm. This is close to the overall Ru thickness of 50 nm, suggesting that these multilayer stacks exhibit a nearly coherent Ru lattice along the growth direction and that, correspondingly, the TiN interlayers have a negligible impact on the Ru crystal quality. However, the brown datapoint for d_{TiN} = 0.4 nm indicates a slight decrease to ξ = 39.4 nm. This decrease becomes much more pronounced for d_{TiN} = 0.6, 1.0, and 1.6 nm with ξ = 33.8, 22.6 and 22.5 nm, respectively. Here the values for

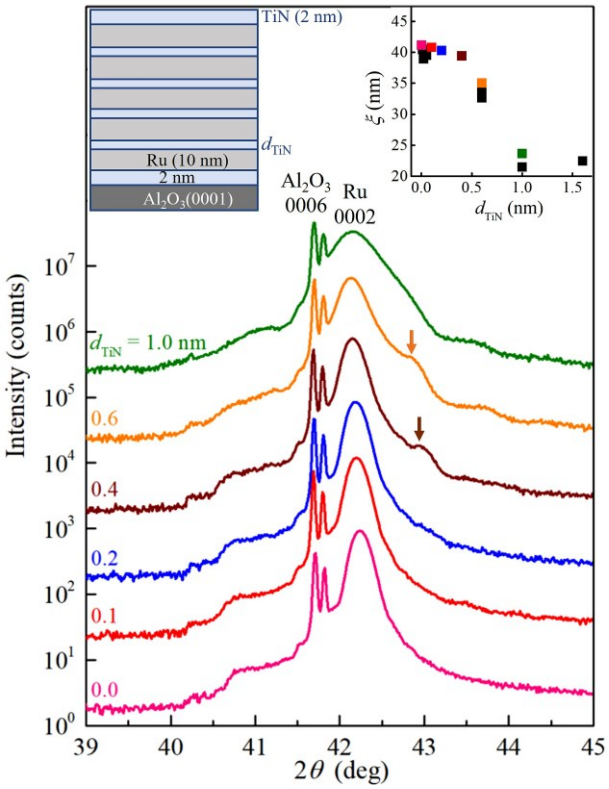

Figure 1. XRD θ-2θ scans from Ru-TiN multilayer films with TiN interlayer thickness d_{TiN} = 0-1 nm, as labeled. The arrows indicate the superlattice satellite peak for d_{TiN} = 0.4 and 0.6 nm. The inset at the top left is a schematic of the Ru-TiN multilayers, with five 10-nm-thick Ru layers, TiN interlayers with thickness d_{TiN} and 2-nm-thick TiN layers at the top and bottom. The inset at the top right is a plot of the x-ray coherence length ξ vs d_{TiN}.

d_{TiN} = 0.6 and 1.0 nm are the average from three and two samples with nominally identical deposition conditions. The observed decrease by a factor of two in ξ is a clear indication that the TiN interlayers with $d_{TiN} \geq 0.4$ nm perturb the coherency of the Ru lattice perpendicular to the interfaces, affecting electron transport between the Ru layers, as discussed below.

Figure 2 shows typical X-ray reflectivity patterns from six multilayer films with d_{TiN} = 0, 0.1, 0.2, 0.4, 0.6 and 1.0 nm. The measured intensity is plotted as solid lines in a logarithmic scale as a function of the scattering angle 2θ = 0.1-5°. The plot includes typical results from direct curve fitting, shown as dotted lines for d_{TiN} = 0.4 and 1.0 nm. The measured critical angle 2θ = 0.92° ± 0.02° for the pure Ru layer (d_{TiN} = 0 nm). It decreases to 0.89° ± 0.02°, 0.87° ± 0.02°, 0.87° ± 0.02°, 0.83 ± 0.02°, 0.79 ± 0.02° with increasing d_{TiN}, indicating a decreasing average multilayer density as a larger fraction of the stack consists of TiN with a density of 5.4 g/cm^3, which is considerably lower than 12.2 g/cm^3 for Ru. The fringes in the plotted intensity are due to the finite total film thickness. They have measured periods of, for example, 0.159°, 0.159° and 0.163° for d_{TiN} = 0.0, 0.1 and 0.2 nm, respectively, yielding total film thicknesses of d = 55.6 ±

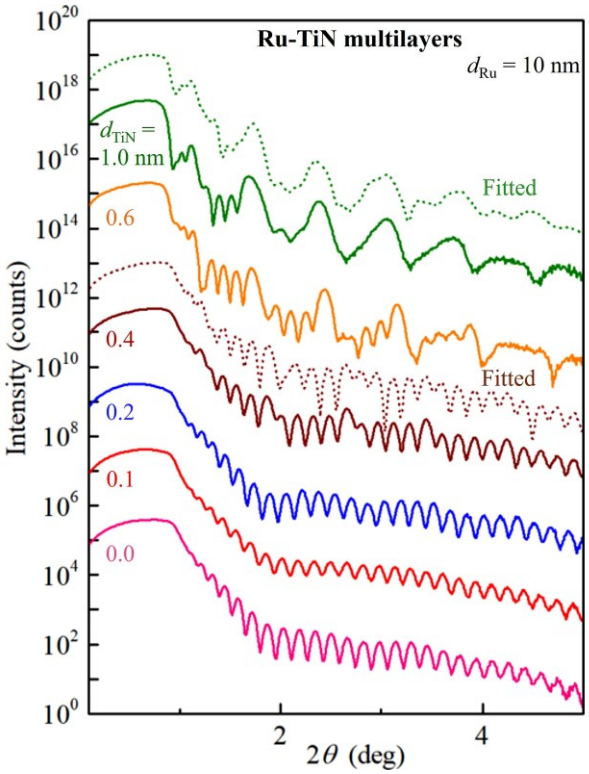

Figure 2. X-ray reflectivity curves from Ru-TiN multilayer films for different TiN interlayer thicknesses d_{TiN} = 0.0-1.0 nm. The dotted lines are the result of curve fitting for d_{TiN} = 0.4 and 1.0 nm.

1.1, 55.6 ± 1.1, 54.1 ± 1.1 nm. The thickness uncertainty is due to an estimated 0.02° uncertainty in the fringe positions. The XRR pattern from the d_{TiN} = 0.4 nm sample is qualitatively different. In addition to the short-period fringes (similar to those observed for $d_{TiN} \leq 0.2$ nm), this pattern exhibits superlattice peaks at $2\theta = 1.86°$, 2.66° and 3.44° which indicate a density modulation with a bilayer thickness Λ = 11.1 ± 0.2 nm. This value is obtained by directly applying Bragg's law and is in good agreement with the expected Λ = 10.4 nm from the deposition rate. The brown dotted line from direct curve fitting indicates good agreement with the measured data from the d_{TiN} = 0.4 nm sample. This data fitting yields a total sample thickness d = 54.5 ± 1.6 nm, which is in excellent agreement with $\Lambda \times 5$ = 55.5 ± 1.0 nm from the superlattice period and 55.6 nm from the deposition rate calibrations. The orange curve in Fig. 2 from the d_{TiN} = 0.6 nm sample is qualitatively similar to the d_{TiN} = 0.4 nm curve. However, the superlattice fringes are much more pronounced, indicating well-developed TiN interlayers between the 10-nm-thick Ru layers. This trend is continued for d_{TiN} = 1.0 nm. The pattern is dominated by broad superlattice peaks at $2\theta = 1.11°$, 1.69°, 2.38°, 3.06°, 3.73°, while the narrow fringes associated with the total film thickness can only be detected for $2\theta < 2°$. Data fitting (green dotted line) yields a total thickness d = 58.3 ± 1.7 nm, in excellent agreement with the expected d = 58.0 nm from deposition rate calibrations. We note that the XRR determination of the total thickness of the multilayer stack is done with multiple methods. More specifically, from (a) the narrow fringes which provide a direct measurement of the total film thickness and is particularly effective for $d_{TiN} \leq 0.4$ nm where the fringes are well resolved, (b) the XRR superlattice fringes which become more pronounced with increasing d_{TiN} and provide a value for the bi-layer period and, in turn, a value for the overall thickness which is accurate for $d_{TiN} \geq 0.4$ nm, and (c) from the deposition rates measured by XRR for a pure Ru and a pure TiN layer and then applied to the multilayer system. Methods (a) and (b) are in good agreement (0.1-3% deviation) with method (c) for small and large d_{TiN}, respectively.

Figure 3 is a plot of the XRD Ru 0002 ω-rocking curve FWHM peak width Γ_ω as a function of the TiN interlayer thickness d_{TiN}. A typical rocking curve is shown in the inset. It is obtained using a fixed $2\theta = 42.20°$ and is used to measure the Ru mosaicity which quantifies the crystalline quality. There is considerable data scatter, particularly for $d_{TiN} \geq 0.6$ nm. Nevertheless, the plot shows a clear general trend of an increasing peak width with increasing d_{TiN}, with Γ_ω = 0.53°, 0.49°, 1.03°, 0.65°, 0.7°, 0.67°, 0.79°, 1°, 1.9°, 1.22°, 1.70°, 1.21°, 1.30° for d_{TiN} = 0, 0.01, 0.02, 0.05, 0.1, 0.2, 0.4, 0.6, 0.6, 0.6, 1.0, 1.0, 1.6 nm, respectively. The increasing width is also evident when comparing the average Γ_ω = 0.69° ± 0.17° for $d_{TiN} \leq 0.2$ nm with Γ_ω = 1.22° ± 0.39° for $d_{TiN} \geq 0.4$ nm, where the latter is nearly two times larger. The increased scatter for d_{TiN} = 0.6 nm together with the increasing Γ_ω between d_{TiN} = 0.4 - 0.6 nm suggests that a critical d_{TiN} = 0.4 - 0.6 nm is required to cause considerable mosaicity and degradation of the Ru crystalline quality.

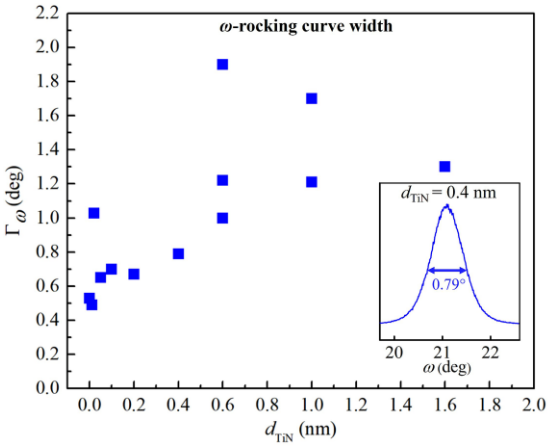

Figure 3. FWHM Γ_ω of ω-rocking curves of the Ru 0002 XRD peak vs TiN interlayer thickness d_{TiN}. The inset shows a representative ω-rocking curve from the d_{TiN} = 0.4 nm mulilayer.

Figure 4 is a plot of the resistivity ρ of Ru-TiN multilayers vs the Ti interlayer thickness. The blue data

points show the measured multilayer resistivity while the red and purple dashed lines are the result from a linear curve fit for $d_{TiN} \leq 0.2$ nm and from a single 10-nm-thick Ru layer, respectively, as discussed below. The first data point shows a 7.80 μΩ-cm resistivity for $d_{TiN} = 0.0$ nm. This sample corresponds to a 50-nm-thick Ru layer sandwicgallhed between two 2-nm-thick top and bottom TiN layers, but without any TiN interlayers. The resistivity is obtained by neglecting transport within the TiN layers, which is expected to be negligible since its sheet conductance is approximately two orders of magnitudes below that of the Ru layers, based on the reported $\rho = 100$ μΩ-cm of 2-nm-thick epitaxial TiN [38]. Thus, the measured $\rho = 7.80$ μΩ-cm corresponds to the resistivity of pure Ru and can be directly compared to the reported $\rho = 7.69$ μΩ-cm for epitaxial Ru(0001)[25]. That is, our pure Ru resistivity matches (within 1.4%) the value for transport in the basal plane of single-crystal Ru(0001) layers, confirming the good crystalline quality of our Ru layers. The plot in Fig. 4 indicates an increasing ρ = 8.00, 9.04, 8.85, 10.92, 11.19, 12.09 μΩ-cm with increasing d_{TiN} = 0.01, 0.02, 0.05, 0.1, 0.2, 0.4 nm. This increase is initially approximately linear, as indicated by the red dashed line which is a linear fit through the data for $d_{TiN} \leq 0.2$ nm. A linear increase is expected for small d_{TiN} where the TiN can effectively be described as an impurity in Ru. That is, for small d_{TiN}, the Ru resistivity increases linearly with an increasing TiN impurity concentration. However, as d_{TiN} is increased to ≥ 0.6 nm, there is (i) a rather large sample-to-sample data spread and (ii) a resistivity saturation for large d_{TiN}. The large scatter in the resistivity data for $d_{TiN} \geq 0.6$ nm is attributed to variations in mosaicity and surface/interface roughness, similar to the large data scatter in the rocking curve width for $d_{TiN} \geq 0.6$ nm presented in Fig. 3. That is, a nominal TiN thickness of 0.6 nm causes a considerable perturbation of the Ru microstructure and may cause the Ru lattice of adjacent Ru layers to be incoherent, consistent with the development of XRR superlattice fringes presented in Fig. 2. More specifically, the three superlattice samples deposited with nominally identical conditions with $d_{TiN} = 0.6$ nm exhibit ρ = 17.94, 16.68, and 14.56 μΩ-cm. The largest value is close to the red dotted line in Fig. 4, which is an extension of the linear impurity-scattering dominated regime. Thus, electron transport in this sample may be best explained by the TiN acting as impurities within Ru. In contrast, the lowest ρ for $d_{TiN} = 0.6$ nm is close to the horizontal dashed line, which corresponds to the measured $\rho = 13.3$ μΩ-cm from a single 10-nm-thick Ru layer which is sandwiched between TiN layers. Thus, electron transport in this (d_{TiN} = 0.6 nm) sample is best described by transport of individual 10-nm-thick Ru layers that are separated by continuous TiN layers. Based on this argument, $d_{TiN} = 0.6$ nm is the critical TiN interlayer thickness where electron transport transitions from TiN acting as impurity within Ru to TiN forming a continuous layer which suppresses coherent electron transport between adjacent Ru layers. Increasing d_{TiN} to 1.0 and 1.6 nm therefore results in continuous TiN layers such that electron transport in these multilayers is best described by parallel conduction in individual 10-nm-thick Ru layers which are separated by TiN interlayers, consistent with the measured resistivity which is close to the horizontal dashed line for an individual 10-nm-thick Ru layer. We note that the intersection of the red and purple lines in Fig. 4 is at d_{TiN} = 0.3-0.4 nm, suggesting a smaller critical thickness than $d_{TiN} = 0.6$ nm obtained with the above argument. Thus, we determine an (average) critical thickness range d_{TiN} = 0.4-0.6 nm from the transport measurements.

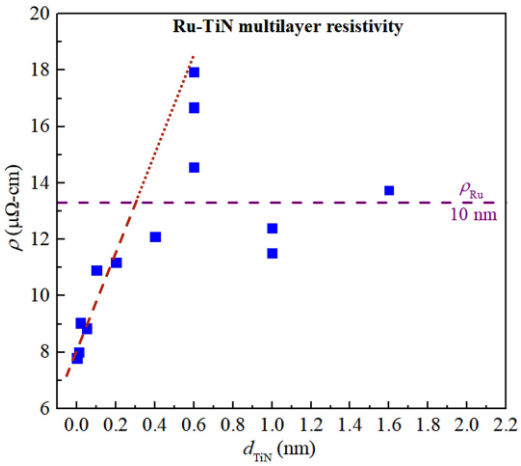

Figure 4. Resistivity ρ vs TiN interlayer thickness d_{TiN} of Ru-TiN multilayer films. The red dashed line indicates the linear increase for $d_{TiN} \leq 0.2$ nm and the purple horizontal line corresponds to $\rho = 13.3$ μΩ-cm measured for an individual 10-nm-thick Ru film.

IV. Conclusions

Sputter deposited Ru-TiN multilayers are used to quantify the effect of TiN interlayers on the Ru resistivity. The resistivity $\rho = 7.8$ μΩ-cm in the absence of TiN interlayers, increases linearly with increasing interlayer thicknegass $d_{TiN} \leq 0.2$ nm, and reaches a saturation ρ = 13.3 μΩ-cm at large $d_{TiN} > 0.6$ nm. The linear increase at small d_{TiN} is attributed to electron scattering at TiN impurities, while transport for large d_{TiN} is independent of d_{TiN} as it is described by parallel conduction in individual 10-nm-thick Ru layers which are separated by continuous TiN interlayers. The data suggest a critical d_{TiN} = 0.4-0.6 nm. Below this critical d_{TiN}, the TiN interlayers are electrically discontinuous, facilitating partially coherent electron transport across neighboring Ru layers while the TiN primarily acts as impurity scattering centers. At larger d_{TiN}, continuous TiN interlayers separate the Ru layers, resulting in diffuse electron scattering at Ru-TiN interfaces without any coherent electron transmission across Ru-TiN-Ru interfaces. The breakdown of the coherent electron transmission above d_{TiN} = 0.4-0.6 nm is attributed to TiN

breaking the translational Ru crystal symmetry. This is consistent with the appearance of an XRD superlattice peak for $d_{TiN} \geq 0.4$ nm, a considerable drop in the out-of-plane x-ray coherence length for $d_{TiN} > 0.4$ nm, and the development of XRR superlattice fringes for $d_{TiN} \geq 0.4$ nm, all confirming that the TiN interlayers with $d_{TiN} \geq 0.4$ nm perturb the coherency of the Ru lattice perpendicular to the interfaces. These data demonstrate that the use of TiN liners for adhesion of Ru interconnects have a negative impact on the via-to-line contact resistance even if the TiN is discontinuous and/or very thin. Thus, a metallization scheme which requires no barrier/liner layer still represents a conductance advantage over a solution which requires a thin (<0.2 nm) liner.

References

[1] H. Kim, "Recent Trends in Copper Metallization," *Electronics*, vol. 11, no. 18, p. 2914, Sep. 2022, doi: 10.3390/electronics11182914.

[2] J. H. Moon, E. Jeong, S. Kim, T. Kim, E. Oh, K. Lee, H. Han, and Y. K. Kim, "Materials Quest for Advanced Interconnect Metallization in Integrated Circuits," *Adv. Sci.*, vol. 10, no. 23, pp. 1–30, Aug. 2023, doi: 10.1002/advs.202207321.

[3] S. M. Rossnagel and T. S. Kuan, "Alteration of Cu conductivity in the size effect regime," *J. Vac. Sci. Technol. B*, vol. 22, no. 1, pp. 240–247, 2004, doi: 10.1116/1.1642639.

[4] D. Gall, "Metals for Low-Resistivity Interconnects," in *2018 IEEE International Interconnect Technology Conference (IITC)*, Jun. 2018, pp. 157–159, doi: 10.1109/IITC.2018.8456810.

[5] S. Dutta, K. Moors, M. Vandemaele, and C. Adelmann, "Finite Size Effects in Highly Scaled Ruthenium Interconnects," *IEEE Electron Device Lett.*, vol. 39, no. 2, pp. 268–271, 2018, doi: 10.1109/LED.2017.2788889.

[6] D. Gall, J. J. Cha, Z. Chen, H. J. Han, C. Hinkle, J.A. Robinson, R. Sundararaman, R. Torsi, "Materials for interconnects," *MRS Bull.*, vol. 46, p. 959, 2021, doi: 10.1557/s43577-021-00192-3.

[7] C. Durkan and M. Welland, "Size effects in the electrical resistivity of polycrystalline nanowires," *Phys. Rev. B - Condens. Matter Mater. Phys.*, vol. 61, no. 20, pp. 14215–14218, 2000, doi: 10.1103/PhysRevB.61.14215.

[8] W. Steinhögl, G. Schindler, G. Steinlesberger, and M. Engelhardt, "Size-dependent resistivity of metallic wires in the mesoscopic range," *Phys. Rev. B - Condens. Matter Mater. Phys.*, vol. 66, no. 7, pp. 1–4, 2002, doi: 10.1103/PhysRevB.66.075414.

[9] R. L. Graham, G. B. Alers, T. Mountsier, N. Shamma, S. Dhuey, S. Cabrini, R. H. Geiss, D. T. Read, "Resistivity dominated by surface scattering in sub-50 nm Cu wires," *Appl. Phys. Lett.*, vol. 96, p. 042116, 2010, doi: 10.1063/1.3292022.

[10] S. S. Ezzat, P. D. Mani, A. Khaniya, W. Kaden, D. Gall, K. Barmak, K. R. Coffey, "Resistivity and surface scattering of (0001) single crystal ruthenium thin films," *J. Vac. Sci. Technol. A*, vol. 37, no. 3, p. 031516, 2019, doi: 10.1116/1.5093494.

[11] P. Y. Zheng, R. P. Deng, and D. Gall, "Ni doping on Cu surfaces: Reduced copper resistivity," *Appl. Phys. Lett.*, vol. 105, no. 13, p. 131603, Sep. 2014, doi: 10.1063/1.4897009.

[12] T. Zhou and D. Gall, "Resistivity scaling due to electron surface scattering in thin metal layers," *Phys. Rev. B*, vol. 97, p. 165406, Apr. 2018, doi: 10.1103/PhysRevB.97.165406.

[13] J. S. Chawla and D. Gall, "Epitaxial Ag(001) grown on MgO(001) and TiN(001): Twinning, surface morphology, and electron surface scattering," *J. Appl. Phys.*, vol. 111, no. 4, pp. 1–10, 2012, doi: 10.1063/1.3684976.

[14] J. S. Chawla, X. Y. Zhang, and D. Gall, "Epitaxial TiN(001) wetting layer for growth of thin single-crystal Cu(001)," *J. Appl. Phys.*, vol. 110, no. 4, pp. 1–5, 2011, doi: 10.1063/1.3624773.

[15] S. Maîtrejean, R. Gers, T. Mourier, A. Toffoli, and G. Passemard, "Experimental measurements of electron scattering parameters in Cu narrow lines," *Microelectron. Eng.*, vol. 83, no. 11–12, pp. 2396–2401, 2006, doi: 10.1016/j.mee.2006.10.044.

[16] E. Milosevic, S. Kerdsongpanya, M. E. Mcgahay, B. Wang, and D. Gall, "The Resistivity Size Effect in Epitaxial Nb(001) and Nb(011) Layers," *IEEE Trans. Electron Devices*, vol. 66, no. 8, pp. 3473–3478, 2019, doi: 10.1109/TED.2019.2924312.

[17] E. Milosevic and D. Gall, "Electron scattering at Co(0001) surfaces: Effects of Ti and TiN capping layers," *AIP Adv.*, vol. 10, p. 055213, 2020, doi: 10.1063/1.5145327.

[18] P. Zheng, T. Zhou, and D. Gall, "Electron channeling in TiO2 coated Cu layers," *Semicond. Sci. Technol*, vol. 31, p. 055005, 2016, doi: 10.1088/0268-1242/31/5/055005.

[19] I. Bakonyi, "Accounting for the resistivity contribution of grain boundaries in metals: critical analysis of reported experimental and theoretical data for Ni and Cu," *Eur. Phys. J. Plus*, vol. 136, no. 4, p. 410, Apr. 2021, doi: 10.1140/epjp/s13360-021-01303-4.

[20] T. Sun, B. Yao, A. P. Warren, K. Barmak, M. F. Toney, R. E. Peale and K. R. Coffey, "Dominant role of grain boundary scattering in the resistivity of nanometric Cu films," *Phys. Rev. B*, vol. 79, p. 041402, 2009, doi: 10.1103/PhysRevB.79.041402.

[21] W. Wu, S. H. Brongersma, M. Van Hove, and K. Maex, "Influence of surface and grain-boundary scattering on the resistivity of copper in reduced dimensions," *Appl. Phys. Lett.*, vol. 84, no. 15, pp. 2838–2840, 2004, doi: 10.1063/1.1703844.

[22] J. S. Chawla, F. Gstrein, K. P. O. Brien, J. S. Clarke, and D. Gall, "Electron scattering at surfaces and grain boundaries in Cu thin films and wires," *Phys. Rev. B*, vol. 84, pp. 235423–1, 2011, doi: 10.1103/PhysRevB.84.235423.

[23] M. César, D. Gall, and H. Guo, "Reducing Grain-Boundary Resistivity of Copper Nanowires by Doping," *Phys. Rev. Appl.*, vol. 5, p. 054018, 2016, doi: 10.1103/PhysRevApplied.5.054018.

[24] M. César, D. Liu, D. Gall, and H. Guo, "Calculated Resistances of Single Grain Boundaries in Copper," *Phys. Rev. Appl.*, vol. 2, p. 044007, 2014, doi: 10.1103/PhysRevApplied.2.044007.

[25] E. Milosevic, S. Kerdsongpanya, A. Zangiabadi, K. Barmak, K. R. Coffey, and D. Gall, "Resistivity Size Effect in Epitaxial Ru(0001) Layers," *J. Appl. Phys.*, vol. 124, no. 16, p. 165105, 2018, doi: 10.1063/1.5046430.

[26] M. Zhang and D. Gall, "Resistivity Scaling in Epitaxial CuAl 2 (001) Layers," *IEEE Trans. Electron Devices*, vol. 69, no. 9, pp. 5110–5115, Sep. 2022, doi: 10.1109/TED.2022.3188952.

[27] M. Zhang, S. Kumar, R. Sundararaman, and D. Gall, "Resistivity scaling in CuTi determined from transport measurements and first-principles simulations," *J. Appl. Phys.*, vol. 133, no. 4, p. 045102, Jan. 2023, doi: 10.1063/5.0135132.

[28] P. Zheng, B. D. Ozsdolay, and D. Gall, "Epitaxial growth of tungsten layers on MgO(001)," *J. Vac. Sci. Technol. A Vacuum, Surfaces, Film.*, vol. 33, no. 6, p. 061505, Nov. 2015, doi: 10.1116/1.4928409.

[29] D. Gall, "The search for the most conductive metal for narrow interconnect lines," *J. Appl. Phys.*, vol. 127, p. 050901, 2020, doi: 10.1063/1.5133671.

[30] D. Gall, "Electron mean free path in elemental metals," *J. Appl. Phys.*, vol. 119, p. 085101, 2016, doi: 10.1063/1.4942216.

[31] E. Milosevic, S. Kerdsongpanya, and D. Gall, "The Resistivity Size Effect in Epitaxial Ru(0001) and Co(0001) Layers," in *2018 IEEE Nanotechnology Symposium, ANTS 2018*, 2019, no. 0001, pp. 1–5, doi: 10.1109/NANOTECH.2018.8653560.

[32] L. G. Wen, P. Roussel, O. V. Pedreira, B. Briggs, B. Groven, S. Dutta, M. I. Popovici, N. Heylen, I. Ciofi, K. Vanstreels, F. W. Østerberg, O. Hansen, D. H. Petersen, K. Opsomer, C. Detavernie, C. J. Wilson, S. V. Elshocht, K. Croes, J. Bömmels, Z. Tőkei, and C. Adelmann, "Atomic Layer Deposition of Ruthenium with TiN Interface for Sub-10 nm Advanced Interconnects beyond Copper," *ACS Appl. Mater. Interfaces*, vol. 8, p. 26119, 2016, doi: 10.1021/acsami.6b07181.

[33] K. V Sagi, H. P. Amanapu, S. R. Alety, and S. V Babu, "Potassium Permanganate-Based Slurry to Reduce the Galvanic Corrosion of the Cu / Ru / TiN Barrier Liner Stack during CMP in the BEOL Interconnects," *ECS J. Solid State Sci. Technol.*, vol. 5, p. 256, 2016, doi: 10.1149/2.0141605jss.

[34] A. E. Kaloyeros and E. Eisenbraun, "Ultrathin Diffusion Barriers/Liners for Gigascale Copper Metallization," *Annu. Rev. Mater. Sci.*, vol. 30, no. 1, pp. 363–385, Aug. 2000, doi: 10.1146/annurev.matsci.30.1.363.

[35] P. Shen and D. Gall, "Electron scattering at interfaces in epitaxial W(001)-Mo(001) multilayers," *J. Appl. Phys.*, vol. 136, p. 075305, 2024, doi: 10.1063/5.0223176.

[36] A. Jog, P. Zheng, T. Zhou, and D. Gall, "Anisotropic Resistivity Size Effect in Epitaxial Mo(001) and Mo(011) Layers," *Nanomaterials*, vol. 13, p. 957, 2023, doi: 10.3390/nano13060957.

[37] F. M. Smits, "Measurement of Sheet Resistivities with the Four-Point Probe," *Bell Syst. Tech. J.*, vol. 37, no. 3, pp. 711–718, May 1958, doi: 10.1002/j.1538-7305.1958.tb03883.x.

[38] J. S. Chawla, X. Y. Zhang, and D. Gall, "Effective electron mean free path in TiN(001)," *J. Appl. Phys.*, vol. 113, no. 6, p. 063704, 2013, doi: 10.1063/1.4790136.